

# Endo-lysosomal A $\beta$ concentration and pH trigger formation of A $\beta$ oligomers that potently induce Tau missorting

Marie P. Schützmann<sup>1,6</sup>, Filip Hasecke<sup>1,6</sup>, Sarah Bachmann<sup>2,6</sup>, Mara Zielinski<sup>3</sup>, Sebastian Hänsch<sup>4</sup>, Gunnar F. Schröder<sup>3,5</sup>, Hans Zempel<sup>2</sup>✉ & Wolfgang Hoyer<sup>1,3</sup>✉

Amyloid- $\beta$  peptide (A $\beta$ ) forms metastable oligomers >50 kDa, termed A $\beta$ O<sub>s</sub>, that are more effective than A $\beta$  amyloid fibrils at triggering Alzheimer's disease-related processes such as synaptic dysfunction and Tau pathology, including Tau mislocalization. In neurons, A $\beta$  accumulates in endo-lysosomal vesicles at low pH. Here, we show that the rate of A $\beta$ O assembly is accelerated 8,000-fold upon pH reduction from extracellular to endo-lysosomal pH, at the expense of amyloid fibril formation. The pH-induced promotion of A $\beta$ O formation and the high endo-lysosomal A $\beta$  concentration together enable extensive A $\beta$ O formation of A $\beta$ 42 under physiological conditions. Exploiting the enhanced A $\beta$ O formation of the dimeric A $\beta$  variant dimA $\beta$  we furthermore demonstrate targeting of A $\beta$ O<sub>s</sub> to dendritic spines, potent induction of Tau missorting, a key factor in tauopathies, and impaired neuronal activity. The results suggest that the endosomal/lysosomal system is a major site for the assembly of pathomechanistically relevant A $\beta$ O<sub>s</sub>.

<sup>1</sup>Institut für Physikalische Biologie, Heinrich-Heine-Universität Düsseldorf, Düsseldorf, Germany. <sup>2</sup>Institute of Human Genetics and Center for Molecular Medicine Cologne (CMMC), University of Cologne, Faculty of Medicine and University Hospital Cologne, Cologne, Germany. <sup>3</sup>Institute of Biological Information Processing (IBI-7) and JuStruct: Jülich Center for Structural Biology, Forschungszentrum Jülich, Jülich, Germany. <sup>4</sup>Department of Biology, Center for Advanced Imaging (CAi), Heinrich-Heine-Universität Düsseldorf, Düsseldorf, Germany. <sup>5</sup>Physics Department, Heinrich-Heine-Universität Düsseldorf, Düsseldorf, Germany. <sup>6</sup>These authors contributed equally: Marie P. Schützmann, Filip Hasecke, Sarah Bachmann. ✉email: [hans.zempel@uk-koeln.de](mailto:hans.zempel@uk-koeln.de); [wolfgang.hoyer@hhu.de](mailto:wolfgang.hoyer@hhu.de)

**A** $\beta$  amyloid fibrils are highly stable protein aggregates of regular cross- $\beta$  structure that constitute the main component of the senile plaques in the brains of Alzheimer's disease (AD) patients<sup>1–3</sup>. Although amyloid fibrils can exert toxic activities, metastable A $\beta$  oligomers are thought to represent the main toxic species in AD<sup>3–5</sup>. At sufficiently high monomer concentration, A $\beta$  readily forms oligomers with molecular weights (MWs) >50 kDa with spherical, curvilinear, and annular shapes, where the elongated structures appear as “beads-on-a-string”-like assemblies of spherical oligomers<sup>4–11</sup>. While multiple names have been given to these metastable A $\beta$  oligomers, including A $\beta$ O, ADDLs, and protofibrils, they seem to be closely related with regard to their structures and detrimental activities and likely form along a common pathway<sup>6,7,12</sup>. Importantly, this pathway is distinct from that of amyloid fibril formation, i.e., A $\beta$ O are not intermediates on the pathway to amyloid fibrils (they are “off-pathway”) but constitute an alternative A $\beta$  assembly type with distinct toxic activities (Fig. 1a)<sup>4,5,11,13</sup>. The distinct nature of A $\beta$  amyloid fibrils and A $\beta$ O is also reflected in their different formation kinetics. A $\beta$  amyloid fibrils form by nucleated polymerization with crucial contributions from secondary nucleation processes, resulting in the characteristic sigmoidal growth time courses that feature an extended lag time<sup>14</sup>. A $\beta$ O, on the other hand, form in a lag-free oligomerization reaction that has a substantially higher monomer concentration dependence than amyloid fibril formation<sup>11</sup>. We note that in this work the term A $\beta$ O refers exclusively to these off-pathway oligomers and does not include other oligomeric A $\beta$  species, such as those transiently formed on the pathway to amyloid fibrils, through secondary nucleation, or through shedding by fibril fragmentation<sup>15</sup>.

Several lines of evidence support a critical role of A $\beta$ O in AD pathogenesis. A $\beta$ O of sizes >50 kDa are the main soluble A $\beta$

species in biological samples<sup>16</sup>. They are synaptotoxic, disrupt long-term potentiation, and cause cognitive impairment in mouse and non-human primate models<sup>4,8,17–23</sup>. Furthermore, A $\beta$ O induce oxidative stress, endoplasmic reticulum stress, neuroinflammation, and elicit Tau missorting, the earliest hallmark of tauopathy in AD<sup>21,23–29</sup>. The detrimental effects are enhanced by pathogenic A $\beta$  mutations that specifically promote A $\beta$ O formation, in particular the arctic (A $\beta$  E22G) and the Osaka (A $\beta$   $\Delta$ E22) mutations<sup>22,23,28,30,31</sup>. Consequently, targeting A $\beta$ O therapeutically is an important alternative to amyloid-centric approaches and has entered clinical evaluation<sup>32–34</sup>.

A $\beta$ O were suggested to trigger toxic effects through ligand-like binding to a remarkably high number of candidate receptors<sup>4,35</sup>. A $\beta$ O achieve clustering of receptors in cell surface signaling platforms, probably promoted by the multivalency inherent to A $\beta$ O<sup>4,35,36</sup>. A $\beta$ O clustering is especially prominent at dendritic spines, which deteriorate upon prolonged exposure to A $\beta$ O<sup>18</sup>. Importantly, this effect is mediated by Tau protein, providing a connection between the A $\beta$  and the Tau aspects of AD pathogenesis. A $\beta$ O induce missorting of Tau into the somatodendritic compartment as well as Tau hyperphosphorylation, leading to microtubule destabilization and spine loss<sup>23,37–39</sup>.

In addition to receptor binding of extracellular A $\beta$ O, intracellular A $\beta$ O are thought to contribute to AD pathogenesis<sup>40</sup>. The endosomal–lysosomal system is the main site not only for A $\beta$  production but also for the uptake of A $\beta$  monomers and A $\beta$ O<sup>27,41–49</sup>. A $\beta$  accumulates in endosomes/lysosomes, which promotes aggregation with potential consequences for cellular homeostasis as well as for the spreading of A $\beta$  pathology by exocytosis of aggregated A $\beta$  species<sup>27,28,41,44–46,48–51</sup>.

At neutral pH, high A $\beta$  concentrations are required to convert a substantial fraction of the protein into A $\beta$ O. Widely used protocols for A $\beta$ O preparation start from around 100  $\mu$ M A $\beta$

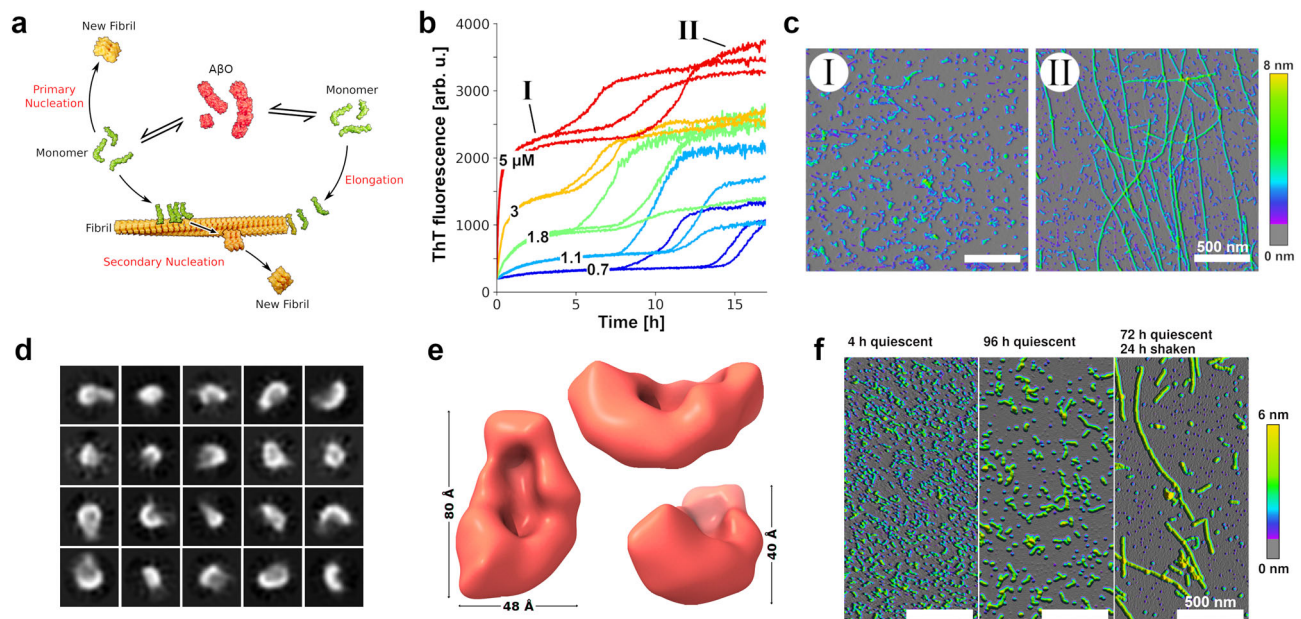


**Fig. 1** A $\beta$ O assemble from dimA $\beta$  in a lag-free oligomerization reaction. **a** Scheme of A $\beta$ O and amyloid fibril formation. **b** Biphasic assembly kinetics of dimA $\beta$  at pH 7.4 and indicated concentrations monitored by ThT fluorescence. The experimental replicates illustrate the good reproducibility of the nucleation-free oligomerization phase and the stochastic nature of the nucleation-dependent fibril growth phase. **c** AFM images corresponding to the two kinetic phases as indicated in **b**. **d** Exemplary 2D classes of the smallest dimA $\beta$  A $\beta$ O species observed in cryo-EM micrographs. **e** 3D density reconstruction of this dimA $\beta$  A $\beta$ O species at a resolution of 17 Å by cryo-EM. The comparatively low resolution is due to the small size and high degree of heterogeneity of the dimA $\beta$  A $\beta$ O species. Consequently, only a rough estimate to size and volume can be made. **f** AFM images of dimA $\beta$  assemblies formed upon incubation at pH 7.4 in microcentrifuge tubes. Kinetics data as shown in **b** was obtained from at least three independently prepared assays with two to three replicates for each concentration for reproducibility. AFM images in **c** were prepared from two independent assays and at least three areas at different positions on the mica surface were scanned. The experiment in **f** was done once and at least two sections of the mica surface were scanned.

monomers<sup>7,8,10</sup>. At tenfold lower A $\beta$  concentration, the formation of A $\beta$ O is already greatly disfavored, which enables the investigation of the pure sigmoidal time course of amyloid fibril formation, including the analysis of on-pathway oligomer formation<sup>14,15,52</sup>. These on-pathway oligomers, however, are short-lived, rapidly consumed in the process of fibril formation, and, as evident from the different assembly kinetics, clearly distinct from the neurotoxic off-pathway A $\beta$ O introduced above. To investigate A $\beta$ O formation, we have generated a dimeric variant of A $\beta$  termed dimA $\beta$ , in which two A $\beta$ 40 units are linked in one polypeptide chain through a flexible glycine–serine-rich linker<sup>11</sup>. In dimA $\beta$ , the conformational properties of the A $\beta$ 40 units are not altered as compared to free A $\beta$ 40 monomers<sup>11</sup>. The linkage of two A $\beta$  units, however, increases the local A $\beta$  concentration, which strongly promotes the highly concentration-dependent formation of A $\beta$ O<sup>11</sup> (Fig. 1b, c). The advantages in applying dimA $\beta$  for the study of A $\beta$ O are: First, A $\beta$ O form already above a threshold concentration (critical oligomer concentration (COC)) of  $\sim 1.5 \mu\text{M}$  dimA $\beta$  at neutral pH. Second, the increased local A $\beta$  concentration preferentially accelerates A $\beta$ O formation as compared to A $\beta$  fibril formation, resulting in an enhanced separation of the kinetic phases of A $\beta$ O and A $\beta$  fibril formation, which facilitates analysis.

There is an apparent discrepancy between the obvious pathogenic relevance of A $\beta$ O and the high  $\mu\text{M}$  A $\beta$  concentrations required for the conversion of a substantial fraction of the protein into A $\beta$ O at neutral pH in vitro, which exceeds the estimated picomolar to nanomolar concentrations of extracellular A $\beta$  in normal brain by several orders of magnitude<sup>44</sup>. However, accumulation of A $\beta$  in the endo-lysosomal system was shown to result in micromolar A $\beta$  concentrations in late endosomes and lysosomes<sup>44</sup>, suggesting that these acidic vesicles might be the prime sites of A $\beta$ O formation. Acidic conditions have been reported to accelerate A $\beta$  aggregation<sup>53</sup>. Here we applied dimA $\beta$  and A $\beta$ 42 to test whether pH reduction from neutral to endo-lysosomal pH affects A $\beta$ O formation. We find that endo-lysosomal pH in fact strongly accelerates A $\beta$ O formation, whereas amyloid fibril formation is delayed, suggesting that A $\beta$ O formation is the dominant aggregation process in endosomes/lysosomes. We furthermore show that dimA $\beta$  is a disease-relevant model construct for pathogenic A $\beta$ O formation by demonstrating that dimA $\beta$  A $\beta$ O target dendritic spines, induce AD-like somatodendritic Tau missorting, and reduce synaptic transmission in terminally matured primary neurons. This indicates that dimA $\beta$ -derived oligomers are suitable for the study of downstream mechanistic and neuropathological events in the progression of AD.

## Results

**DimA $\beta$  assembles into A $\beta$ O that bind to dendritic spines and potently induce Tau missorting.** The assembly kinetics of dimA $\beta$  at neutral pH monitored by ThT show a biphasic behavior above a concentration (COC) of  $\sim 1.5 \mu\text{M}$ , with the first phase corresponding to the lag-free oligomerization into A $\beta$ O and the second phase reflecting amyloid fibril formation<sup>11</sup> (Fig. 1b, c). DimA $\beta$  A $\beta$ O are of spherical and curvilinear shape (Fig. 1c) and rich in  $\beta$ -structure<sup>11</sup>, in agreement with the characteristics of A $\beta$ O formed from A $\beta$ 40 and A $\beta$ 42 (refs. 4–6,9,13,21; for atomic force microscopic (AFM) data of A $\beta$ O formed from A $\beta$ 42, see below). We applied cryogenic electron microscopy (cryo-EM) to further characterize dimA $\beta$  A $\beta$ O structurally. Structure determination is hampered by the size and shape heterogeneity of A $\beta$ O<sup>7,9,10</sup>, which is moreover evolving with time, as observed for A $\beta$ O formed from A $\beta$ <sup>9</sup> as well as dimA $\beta$ <sup>11</sup>. As larger A $\beta$ O seem to be assemblies of small spherical structures, our analysis focused

on the small A $\beta$ O observed in the micrographs (Fig. 1d, e and Supplementary Figs. 1–3). The fraction of small A $\beta$ O was  $72 \pm 12\%$  in terms of particle number but only  $\sim 2\text{--}3\%$  in terms of the number of A $\beta$  molecules within A $\beta$ O (Supplementary Fig. 1c). The relation between the small and the elongated curvilinear A $\beta$ O cannot be inferred from the micrographs. Nevertheless, structure elucidation of the small A $\beta$ O could provide insight into a biologically relevant A $\beta$ O substructure that may furthermore laterally associate and convert into protofibrillar A $\beta$ O<sup>54</sup>. We obtained a three-dimensional (3D) density reconstruction (Fig. 1e) at a resolution of 17 Å, which shows a bowl-shaped structure with dimensions of  $80 \times 48 \times 40$  Å. From this reconstruction, we were able to calculate the approximate molecular mass that fits into the density to be 62 kDa (Supplementary Fig. 3; see “Methods”). Therefore, the small A $\beta$ O species, as visible on the micrographs, likely contains six dimA $\beta$  monomers (total MW of 60.2 kDa), which corresponds to 12 A $\beta$ 40 units. Dodecameric A $\beta$  oligomers were observed before in A $\beta$ O preparations from synthetic peptide or isolated from AD brain or mouse models and have been associated with neuronal dysfunction and memory impairment<sup>55–58</sup>.

A $\beta$ O formation occurred on the same time scale in the plate reader experiment as in microcentrifuge tubes (Fig. 1b, c, f). In contrast, extensive amyloid formation was observed in the plate reader experiment after  $\sim 10$  h but was not detectable when A $\beta$ O were incubated in microcentrifuge tubes for several days, unless the microcentrifuge tube was agitated (Fig. 1b, c, f). This suggests that the movement of the microplate in the plate reader, caused by scanning of the wells during measurements every 3 min and 2 s of preceding orbital shaking, creates sufficient agitation to promote amyloid fibril nucleation. When the samples in the microplate were covered with a layer of mineral oil, A $\beta$ O formation was unaffected but amyloid fibril formation was completely abrogated (Supplementary Fig. 4), in line with the essential role of the air–water interface in A $\beta$  amyloid formation in vitro<sup>59</sup>. The strong effects of agitation<sup>14</sup> and air–water interface on A $\beta$  amyloid fibril formation but not on A $\beta$ O formation confirms again that their assembly mechanisms are different and is in line with the notion that A $\beta$ O formation does not involve a nucleation step<sup>11,60</sup>. When A $\beta$ O, formed by incubation of dimA $\beta$  above the COC, were diluted to sub-COC concentrations, they persisted for  $>24$  h, indicating high kinetic stability (Supplementary Fig. 5). We conclude that A $\beta$ O formed from dimA $\beta$  under quiescent conditions are kinetically stable, not replaced by amyloid fibrils for several days, and can be applied at sub- $\mu\text{M}$  concentrations. DimA $\beta$  A $\beta$ O may therefore serve as a favorable A $\beta$ O model.

To test whether dimA $\beta$  A $\beta$ O cause the same biological effects as reported for A $\beta$ O formed from A $\beta$ 40 or A $\beta$ 42, we investigated their binding to dendritic spines, their direct cytotoxicity, their capacity to induce Tau missorting, and their consequences for neuronal function. A $\beta$ O were formed from 20  $\mu\text{M}$  dimA $\beta$  and added to primary mouse neurons (days in vitro 15 (DIV15)–22) to a final concentration of 0.5  $\mu\text{M}$  (all dimA $\beta$  A $\beta$ O concentrations given in dimA $\beta$  equivalents). One micromolar A $\beta$ 40 was used as monomeric control. DimA $\beta$  localized to neuronal dendrites both after 3 and 24 h of treatment, where it partially co-localized with dendritic protrusions positive for filamentous actin (stained by phalloidin), which mark synaptic spines (Fig. 2a). In contrast, A $\beta$ 40 monomers did not show substantial localization to dendrites (Fig. 2a). Direct cytotoxicity was assessed by analysis of the sizes and shapes of neuronal nuclei upon staining with NucBlue. The fractions of normal and dense nuclei did not change significantly after incubation with dimA $\beta$  A $\beta$ O (Fig. 2b, c), indicating the absence of direct cytotoxicity, in line with previous reports on A $\beta$ O<sup>61</sup>.

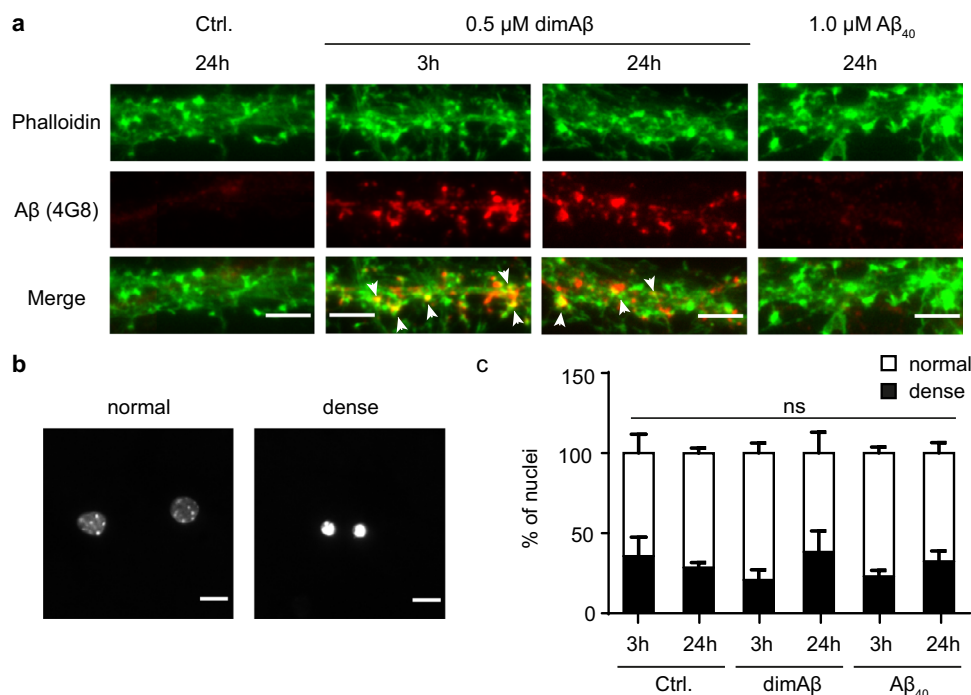


**Fig. 2 DimAβ AβOs bind to dendrites and postsynaptic spines but have no direct cytotoxic effect on primary mouse neurons.** Primary mouse neurons (DIV15–22) were treated with 0.5 μM dimAβ AβOs or 1 μM Aβ<sub>40</sub> for 3 and 24 h. **a** DimAβ AβOs localized to neuronal dendrites both after 3 and 24 h of treatment, where they partially co-localized with phalloidin, a marker for synaptic spines. Arrows indicate co-localization of dimAβ with phalloidin. Scale bar, 5 μm. The experiment was independently repeated four times with similar results. **b** Nuclei of primary neurons were stained with NucBlue and analyzed with respect to shape and size. Representative images of normal and dense nuclei. Scale bar, 10 μm. **c** Quantification of normal and dense nuclei of primary neurons after vehicle control, Aβ<sub>40</sub>, or dimAβ AβO treatment revealed no direct cytotoxicity. *N* = 3; around 300 nuclei were analyzed for each condition. Error bars represent SEM. Statistical analysis was done by two-way ANOVA with Tukey's test for multiple comparisons and yielded no significant differences between the experimental groups.

Tau cellular distribution was analyzed with an anti-Tau (K9JA) antibody. DimAβ AβO-treated neurons showed strong enhancement of the fluorescence signal of Tau in the soma after 24 h of treatment (Fig. 3), indicating pathological somatodendritic Tau missorting as previously reported for AβOs<sup>38,39</sup>. In contrast, Aβ<sub>40</sub> monomers did not induce Tau missorting in our experimental setting (Fig. 3). In previous studies, Tau missorting and spine loss were reversible within 12–24 h due to loss of AβO potency (transformation of AβOs over time to larger, non-toxic aggregates)<sup>38,62</sup>. Here we observe an increase of Tau missorting over time, which indicates remarkable kinetic stability and persistent ability of dimAβ AβOs to induce pathological Tau missorting.

Next, we investigated the consequences of AβO exposure for neuronal function. As readout, we measured spontaneous calcium oscillations in our neuronal cultures after dimAβ AβO treatment as an indicator for neuronal activity with live-cell imaging, using the fluorescent cell-permeable calcium indicator Fluo-4 as previously described<sup>38</sup>. A significant decrease of calcium oscillations was observed after 24 h but not after 3 h of treatment with dimAβ AβOs (Fig. 4). As calcium oscillations in our conditions depend on action potentials and neurotransmission, this indicates that dimAβ AβOs impair neuronal activity and function. With regard to dendritic spine binding, lack of direct cytotoxicity, potent induction of Tau missorting as well as decreased neuronal activity, dimAβ AβOs thus faithfully reproduce the observations previously made for AβOs formed from Aβ<sub>40</sub> or Aβ<sub>42</sub> or from 7:3 Aβ<sub>40</sub>:Aβ<sub>42</sub> mixtures regarded as particularly toxic<sup>38</sup>. Of note, dimAβ AβOs effects appeared later (24 vs. 3 h) than for the previously studied oligomers, hinting toward their kinetic and structural stability in cell culture conditions.

**Aβ<sub>42</sub> as well as dimAβ accumulate within endo-lysosomal compartments.** Next, we aimed to test the uptake of dimAβ AβOs in neuronal cells. First, SH-SY5Y neuroblastoma cells were subjected to a mixture of 0.1 μM HiLyte Fluor 647-labeled Aβ<sub>42</sub> and 1 μM unlabeled Aβ<sub>42</sub>. After 24 h of incubation, Aβ<sub>42</sub> accumulated within vesicular foci within the cytoplasm of the cells. Co-staining with a LysoTracker dye showed prominent colocalization suggesting the accumulation of Aβ<sub>42</sub> within endo-lysosomal compartments (Fig. 5). This is in line with previous studies that showed Aβ<sub>42</sub> accumulation in acidic vesicles of neuroblastoma cells and primary murine cortical neurons<sup>41,44–46</sup>. Hu et al. measured local Aβ<sub>42</sub> concentrations >2.5 μM within endo-lysosomal compartments, which exceeds the extracellular concentration by approximately four orders of magnitude<sup>44</sup>.

In a second attempt, SH-SY5Y cells were treated with 1.1 μM Abberior Star 520SXP-labeled dimAβ AβOs, formed from a mixture of 91% unlabeled and 9% fluorophore-labeled dimAβ (i.e., same final concentrations of unlabeled and fluorophore-labeled Aβ as in the Aβ<sub>42</sub> experiment above). This experiment revealed a similar colocalization in acidic vesicles as for Aβ<sub>42</sub> (Fig. 5). This confirms that both Aβ monomers and AβOs are readily taken up by neuron-like cells and accumulate in the endo-lysosomal system. Our results, however, do not reveal the assembly state of Aβ, and it is possible that the applied Aβ species undergo structural alterations upon cell entry and accumulation in endo-lysosomes, such as higher-order assembly as described below.

**Endo-lysosomal pH promotes AβO assembly but delays amyloid fibril formation.** Due to the accumulation of Aβ, endosomes/lysosomes might constitute the dominant site of the highly

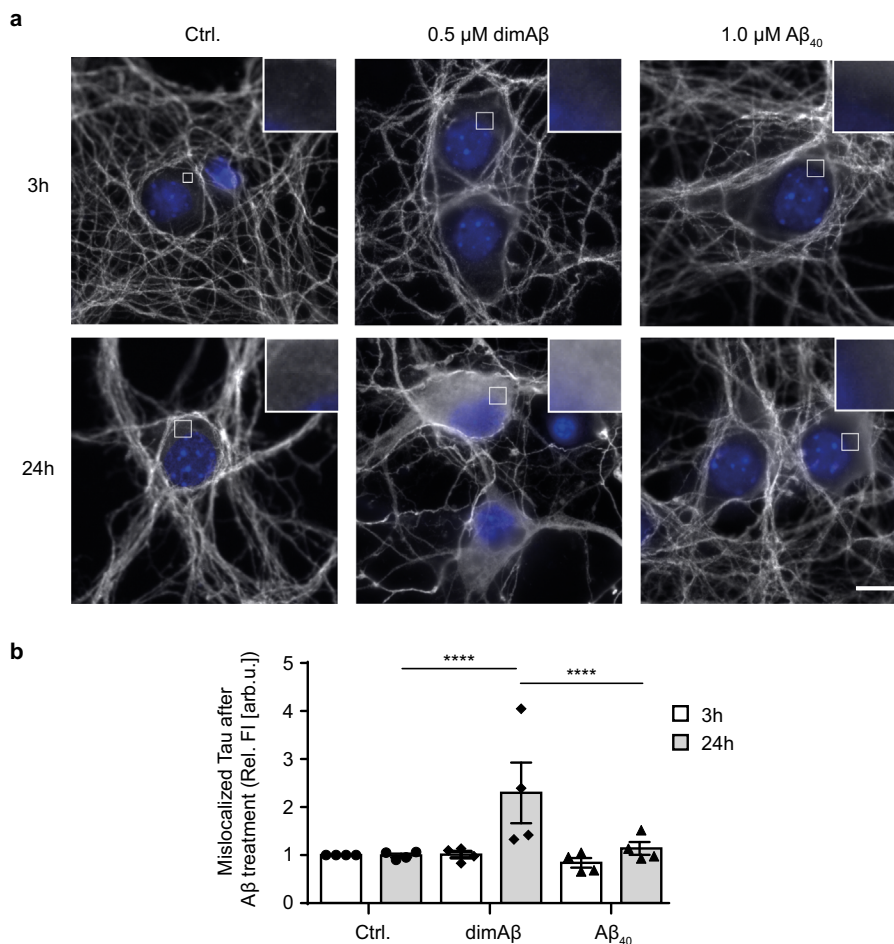


**Fig. 3 DimA $\beta$  A $\beta$ O<sub>s</sub> induce pathological somatodendritic missorting of Tau.** Primary mouse neurons (DIV15–22) were treated with 0.5  $\mu\text{M}$  dimA $\beta$  A $\beta$ O<sub>s</sub> or 1  $\mu\text{M}$  A $\beta_{40}$  for 3 and 24 h. **a** Representative images of cell bodies of primary neurons after treatment with A $\beta$ . Neurons were stained with anti-Tau (K9JA) antibody; nuclei were stained with NucBlue. DimA $\beta$  A $\beta$ O<sub>s</sub>-treated neurons show strong enrichment of fluorescence signal of Tau in the soma after 24 h of treatment. Insets show magnification of white boxed areas in the somata. Scale bar, 10  $\mu\text{m}$ . **b** Quantification of Tau enrichment in the soma of primary neurons. Fluorescence intensities of cell bodies were quantified and normalized to control-treated neurons after 3 h of treatment.  $N = 4$ , 30 cells were analyzed for each condition. Error bars represent SEM. Statistical analysis was done by two-way ANOVA with Tukey's test for multiple comparisons. Statistical significance: \*\*\*\* $p < 0.0001$ .

concentration-dependent A $\beta$ O formation. Apart from the increased A $\beta$  concentration in endosomes/lysosomes, the low pH in late endosomes ( $\sim 5.5$ ) and lysosomes ( $\sim 4.5$ ) might promote A $\beta$ O formation. We used dimA $\beta$  to simultaneously determine the specific effects of pH on A $\beta$ O formation and on amyloid fibril formation. Lyophilized dimA $\beta$  was dissolved in 6 M buffered guanidinium chloride, followed by size-exclusion chromatography (SEC) into 1 mM NaOH, leading to a pH of 10.9, and added to the wells of a microplate. The basic pH conditions prohibit premature aggregation of A $\beta^{63}$ . The pH-dependent aggregation reaction was initiated in the microplate reader by injection of a 10 $\times$  buffer yielding the desired final pH, allowing for monitoring of ThT fluorescence without any substantial delay. We determined the kinetics of dimA $\beta$  assembly between pH 4.8 and 7.6 in the concentration range 0.65–5.0  $\mu\text{M}$ . At neutral pH, the initial kinetic phase reflecting A $\beta$ O formation spanned several hours, but upon pH reduction, A $\beta$ O formation was continuously accelerated and occurred within a few seconds at pH 4.8 (Fig. 6a–g). ThT fluorescence intensity decreased at acidic pH<sup>64</sup> but was still sufficiently sensitive to detect the signal of A $\beta$ O formation at pH 4.8 and 0.65  $\mu\text{M}$  dimA $\beta$  (Fig. 6g). For pH 7.4, we have previously shown that a global fit of an  $n$ th-order oligomerization reaction to the concentration-dependent assembly kinetics is in good agreement with the data and yields a reaction order of  $\sim 3.3$  for

dimA $\beta$  A $\beta$ O formation<sup>11</sup>. Here we found that a reaction order of three applied to global fitting of the concentration-dependent data results in fits that reproduce the kinetic traces at all pH values (Fig. 6a–g). This indicates that the fundamental mechanism of A $\beta$ O formation is not affected by pH reduction. A logarithmic plot of the obtained oligomerization rate constants against pH shows a linear trend with a slope of  $-1.56$ , i.e., the rate constant decreases 36-fold per pH unit within the investigated pH range (Fig. 6h). At pH 4.8, in between lysosomal and endosomal pH, A $\beta$ O formation is 7900-fold faster than at interstitial pH (7.3).

In order to test whether the acceleration of A $\beta$ O formation kinetics is accompanied by thermodynamic stabilization, we evaluated the effect of pH reduction on the COC of dimA $\beta$ . In the A $\beta$ O formation assay at pH 7.4, the fluorescence intensity increase during the lag-free oligomerization phase scaled linearly with protein concentration at dimA $\beta$  concentrations above  $\sim 2$   $\mu\text{M}$ , whereas no lag-free oligomerization was detectable below  $\sim 0.5$   $\mu\text{M}$ , indicative of a COC of around 1  $\mu\text{M}$  (Supplementary Fig. 6a, b). At pH 5.6, however, there is no indication of disappearance of the oligomerization phase down to a concentration of 0.4  $\mu\text{M}$  dimA $\beta$  (Supplementary Fig. 6c, d). Due to the limited sensitivity of ThT at acidic pH<sup>64</sup>, it is not possible to reliably monitor oligomerization at lower concentrations and to

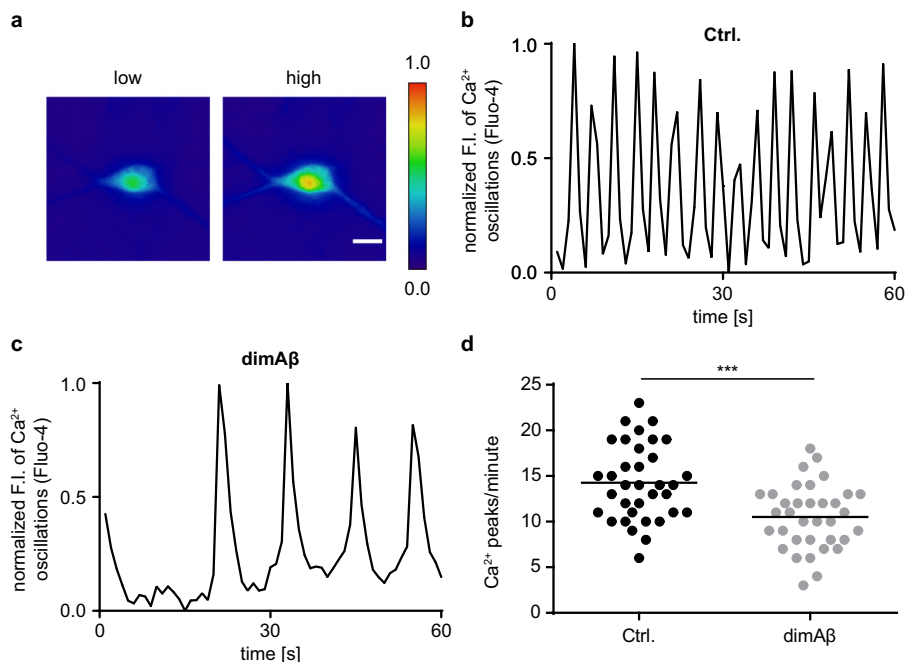


**Fig. 4 DimA $\beta$  A $\beta$ Os decrease spontaneous calcium oscillations of primary mouse neurons.** Primary mouse neurons (DIV15–22) were treated with 0.5  $\mu$ M dimA $\beta$  A $\beta$ Os for 24 h. Cells were labeled with calcium-sensitive Fluo-4 dye and spontaneous calcium oscillations were recorded by time-lapse movies. **a** Representative ratiometric images of low and high calcium concentrations in the soma of a neuron. Scale bar, 20  $\mu$ m. **b, c** Representative graphs of spontaneous Ca $^{2+}$  oscillations in **b** vehicle control- and **c** dimA $\beta$  A $\beta$ O-treated primary neurons. Fluorescence intensities were normalized to minimum values and plotted over time. **d** Quantification of spontaneous Ca $^{2+}$  oscillations in primary neurons after vehicle control or dimA $\beta$  A $\beta$ O treatment. Fluorescence intensities were normalized to minimum values and peaks per minute were counted for each sample. In total, 35 cells were analyzed; statistical analysis was done by two-tailed unpaired *t* test. Statistical significance: \*\*\**p* = 0.0001.

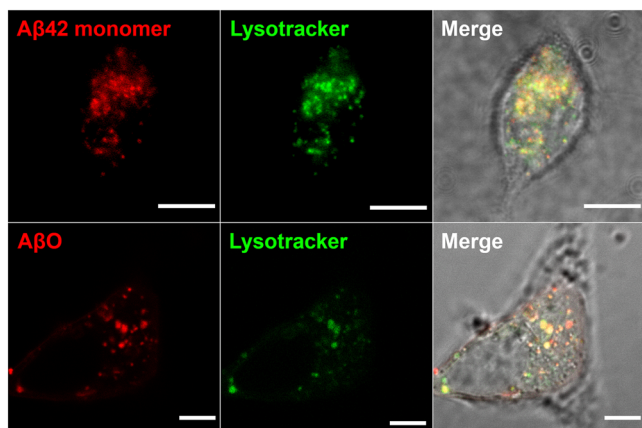


**Fig. 5 A $\beta$ 42 and dimA $\beta$  A $\beta$ Os accumulate in endosomes/lysosomes.** SH-SY5Y cells were treated with A $\beta$ 42 monomers (top row) or dimA $\beta$  A $\beta$ Os (bottom row) and co-localization with endo-lysosomal compartments was analyzed. 1.1  $\mu$ M A $\beta$ 42 (containing 9% HiLyte 647-labeled A $\beta$ 42, top row) or 1.1  $\mu$ M dimA $\beta$  A $\beta$ Os (in monomer equivalents, formed from a dimA $\beta$  solution containing 9% AbberiorStar 520SXP-labeled dimA $\beta$ , bottom row) were added to the cells. After 24 h, the medium was exchanged with fresh medium supplemented with 50 nM Yellow HCK-123 LysoTracker dye. Scale bar, 5  $\mu$ m. *N* = 3, at least three images were acquired for each treatment to ensure reproducibility.

determine the COC at this pH. Nevertheless, the COC at pH 5.6 is clearly lower than the COC at neutral pH, indicative of thermodynamic stabilization of A $\beta$ Os at acidic pH.

A $\beta$ Os formed at different pH values were imaged by AFM (Fig. 6i–o). From pH 7.6 to pH 6.8, A $\beta$ Os were mainly spherical and curvilinear structures, the latter apparently resulting from

bead-chain-like association of the spherical A $\beta$ Os<sup>6</sup>. At pH 6.4, A $\beta$ Os showed an increased tendency to form more compact structures, such as annular protofibrils and denser clusters. Below pH 6.0, A $\beta$ Os associated into large clusters, in line with a previous description of A $\beta$ 40 aggregates at pH 5.8<sup>53</sup>. In AFM, these A $\beta$ O clusters have average heights of ~100 nm, compared to heights of ~4 nm observed for A $\beta$ Os formed between pH 6.0 and 7.2 (Fig. 6p). Thus, while the fundamental mechanism of A $\beta$ O formation seems to be unaffected by pH reduction, there is an additional level of particle aggregation involved below pH 6.0.

The second kinetic phase in the ThT time course of dimA $\beta$  aggregation reports on amyloid fibril formation<sup>11</sup>. It is characterized by a lag time, which reflects the primary and secondary nucleation events involved in nucleated polymerization<sup>14,52</sup>. In contrast to the acceleration of A $\beta$ O formation, the lag time of amyloid formation did not decrease with decreasing pH. On the contrary, the amyloid fibril formation phase could not be observed within 10 h experiments at pH values of 6.8 and below. This can be explained by the inhibition that the rapidly forming A $\beta$ Os entail on amyloid formation: First, A $\beta$ Os compete for the monomer growth substrate of amyloid fibril growth; second, A $\beta$ Os actively inhibit amyloid fibril growth<sup>11,65</sup>.

**A $\beta$ O assembly of A $\beta$ 42 is enabled under endo-lysosomal conditions.** We investigated whether the promotion of A $\beta$ O formation at endo-lysosomal pH is sufficient to also support A $\beta$ O formation from A $\beta$ 42 at relevant endo-lysosomal A $\beta$  concentrations, determined to be well above 2.5  $\mu$ M<sup>44</sup>. At pH 7.2, A $\beta$ 42 in the concentration range 1.9–9  $\mu$ M displayed sigmoidal assembly kinetics typical for amyloid fibril formation (Fig. 7a). The absence of a lag-free oligomerization phase is in agreement with the observation that the COC of A $\beta$ 42 in *in vitro* assay at neutral pH

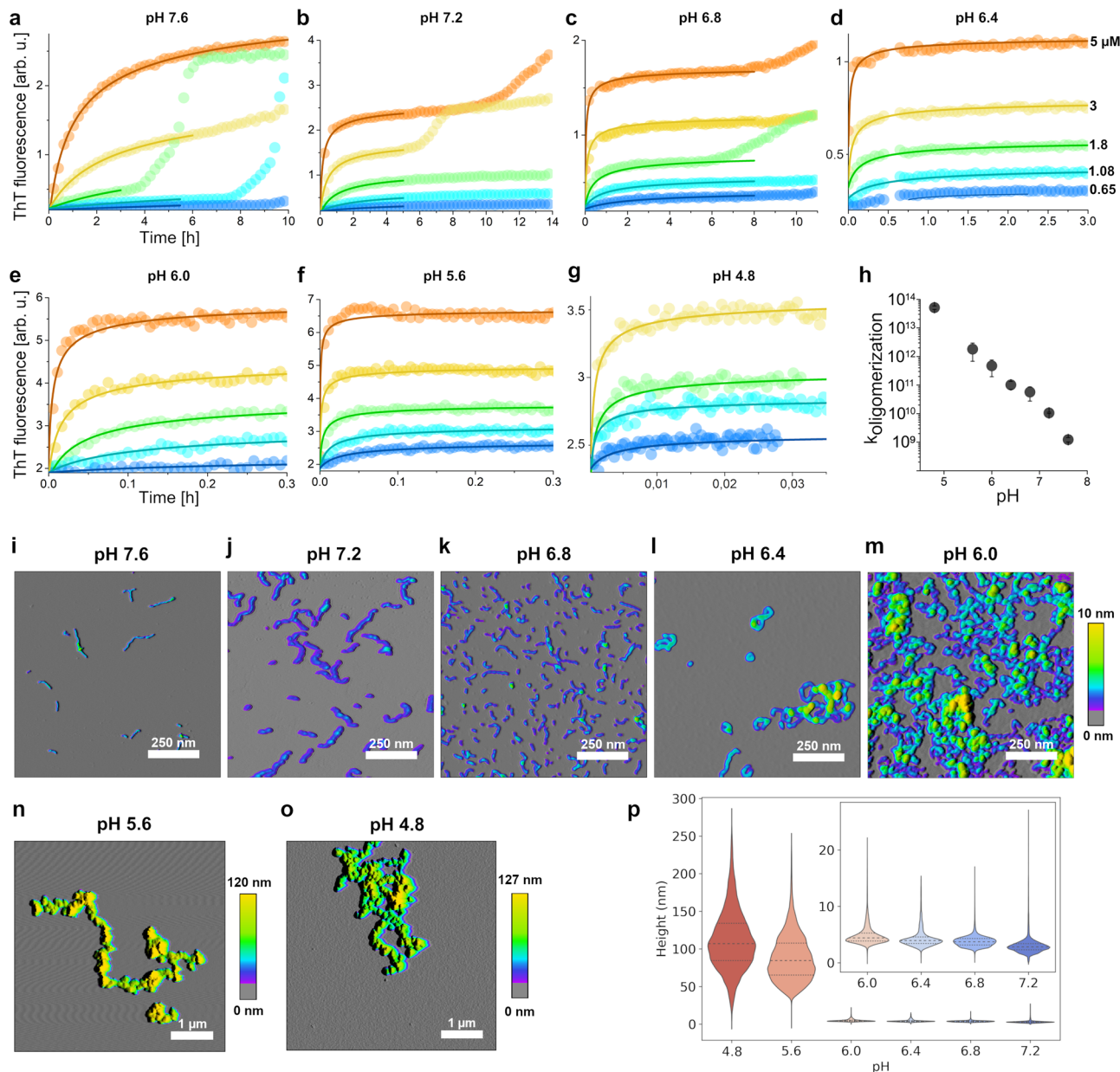


**Fig. 6 pH dependence of dimAβ assembly kinetics.** **a–g** DimAβ assembly at concentrations between 0.65 and 5 μM and at pH values between 4.8 and 7.6 monitored by ThT fluorescence. Solid lines represent global fits to the data using a one-step oligomerization model with a shared reaction order of 3 for all pH values and concentrations and an individual oligomerization rate constant per pH value. **h** Logarithmic plot of the obtained oligomerization rate constants vs. pH. The rate constants were obtained from global fits to *n* concentration dependence data sets obtained from *m* independently prepared assays, with *n/m* being 2/2 (pH 4.8), 6/4 (pH 5.6), 8/4 (pH 6.0), 5/4 (pH 6.4), 6/2 (pH 6.8), 6/2 (pH 7.2), and 6/2 (pH 7.6). One of the *n* repeats is shown in **a–g**. Replicates are given in Supplementary Fig. 8. Data points represent mean and standard deviation, except for pH 4.8, where the error bar indicates the higher and lower value of the *n* = 2 experiments. **i–o** AFM images of dimAβ AβO formed at different pH values. Note the dramatic change in the height scale bar upon pH decrease to <6.0 due to formation of large AβO clusters. Between 7 and 25 micrographs of at least 2 independent assays were recorded for each pH value to ensure reproducibility. **p** Particle height distributions determined from AFM images, displayed as violin plots. All pixels assigned to AβOs by the image analysis software in five micrographs per pH value were evaluated. Dashed lines represent medians; dotted lines represent interquartile ranges. Inset, zoom on the data for pH 6.0 to pH 7.2.

is >10 μM<sup>65</sup>. Consequently, the aggregation products under this condition are amyloid fibrils (Fig. 7c, f). In contrast, at pH 4.5 lag-free aggregation occurred at a concentration of ≥5.4 μM (Fig. 7b). The change from lag-containing to lag-free conditions at pH 4.5 was accompanied by a switch in aggregate morphology from amyloid fibril networks to large AβO clusters identical to those observed for dimAβ at endo-lysosomal pH (Fig. 7d, e, g, h). This indicates that under endo-lysosomal conditions the local Aβ concentration can exceed the COC of AβO formation, suggesting

that endosomes/lysosomes may represent crucial sites of AβO formation in vivo.

Aβ aggregates can leak from endosomes/lysosomes into the cytosol and to other cell compartments or can be secreted and spread to other cells, potentially contributing to the propagation of Aβ pathology<sup>27,28,44,45,51</sup>. Upon transfer from endosomes/lysosomes to the cytosol or interstitial fluid, AβOs experience a shift from acidic to neutral pH. We tested the kinetic stability of AβOs formed at pH 4.5 after a shift to neutral pH by monitoring

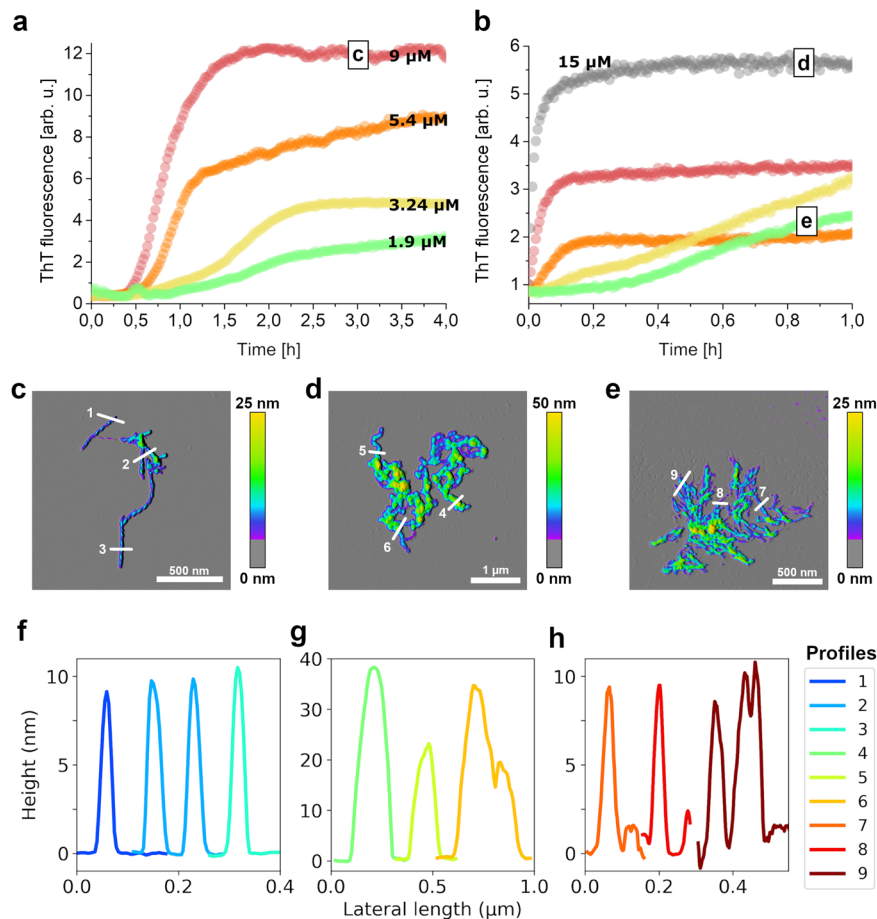


**Fig. 7** Aβ42 rapidly forms AβOs at endo-lysosomal pH. **a, b** Aβ42 assembly at **a** pH 7.2 or **b** pH 4.5 at concentrations between 1.9 and 15 μM monitored by ThT fluorescence. Replicates are given in Supplementary Fig. 9. **c–e** AFM images of **c** amyloid fibrils formed by 9 μM Aβ42 at pH 7.2, **d** AβOs formed by 15 μM Aβ42 at pH 4.5, and **e** amyloid fibril networks formed by 1.9 μM Aβ42 at pH 4.5. At least three micrographs each of two independently prepared sample repeats were recorded to ensure reproducibility of the AFM data. **f–h** Height profiles of the sections indicated in **c–e**.

the ThT intensity and by imaging of the aggregate morphology by AFM. We applied Aβ42 at a concentration of 10 μM in this experiment, as Aβ42 does not form AβOs de novo at this concentration at neutral pH. Any AβOs observed after the pH shift can therefore safely be ascribed to the kinetic stability of AβOs pre-formed under acidic conditions. As before, a pH shift from basic pH to pH 4.5 was applied to initiate AβO formation. After AβO formation had reached a steady state, pH was adjusted to 7.2 by a further injection of a corresponding buffer stock. After the adjustment to neutral pH, there was an instantaneous increase in ThT fluorescence (Supplementary Fig. 7), which can be explained by the pH dependence of ThT fluorescence<sup>64</sup>. Thereafter, the ThT fluorescence did not exhibit any other larger changes that would be expected in the case of disassembly of AβOs or replacement of AβOs by an alternative type of aggregate. Apart from dense clusters like those observed for low pH AβOs, AFM images showed spherical and curvilinear structures typical for AβOs formed at neutral pH, indicating dissociation of the AβO clusters into their constituents (Fig. 8a). In fact, the AFM images suggest that smaller AβOs detach from fraying AβO clusters. The height of the cluster-released Aβ42 AβOs was 3.5–4.5 nm as measured by AFM in the dried state (Fig. 8b, c), identical to that of Aβ42 AβOs (Fig. 8d, e) and dimAβ AβOs (Fig. 6p) that were directly formed at neutral pH. Taken together, the ThT and AFM data demonstrate that AβOs formed at endo-lysosomal pH possess a high kinetic stability after shifting to

neutral pH, which is, however, accompanied by dissociation of large AβO clusters into spherical and curvilinear AβOs.

## Discussion

AβOs have been identified as the main neurotoxic Aβ species in AD. The characterization of the most critical disease-related AβOs has revealed that they are metastable oligomers >50 kDa in size that do not represent intermediates of amyloid fibril formation but are an alternative Aβ assembly type. However, the conditions required for AβO formation and the underlying mechanism have not been elucidated in detail. Here we show that AβO formation is highly pH dependent and is accelerated ~8000-fold upon a change in pH from neutral to endo-lysosomal pH. At the same time, the COC of AβO formation is reduced. This enables AβO formation at physiologically relevant Aβ concentrations, determined to be well above 2.5 μM in endo-lysosomal vesicles<sup>44</sup>. The strong acceleration of AβO formation at pH 4.5–5.5 suggests that the endosomal/lysosomal system might be a major site of AβO formation. AβOs may either form from Aβ monomers that have been newly generated by amyloid precursor protein (APP) processing or from endocytosed monomers (Fig. 9)<sup>40–42,44,47,48</sup>. APP processing in endo-lysosomal compartments by γ-secretase containing presenilin 2 generates a prominent pool of intracellular Aβ that is enriched in Aβ42 (ref. 48). Esbjörner et al. applied fluorescence lifetime and

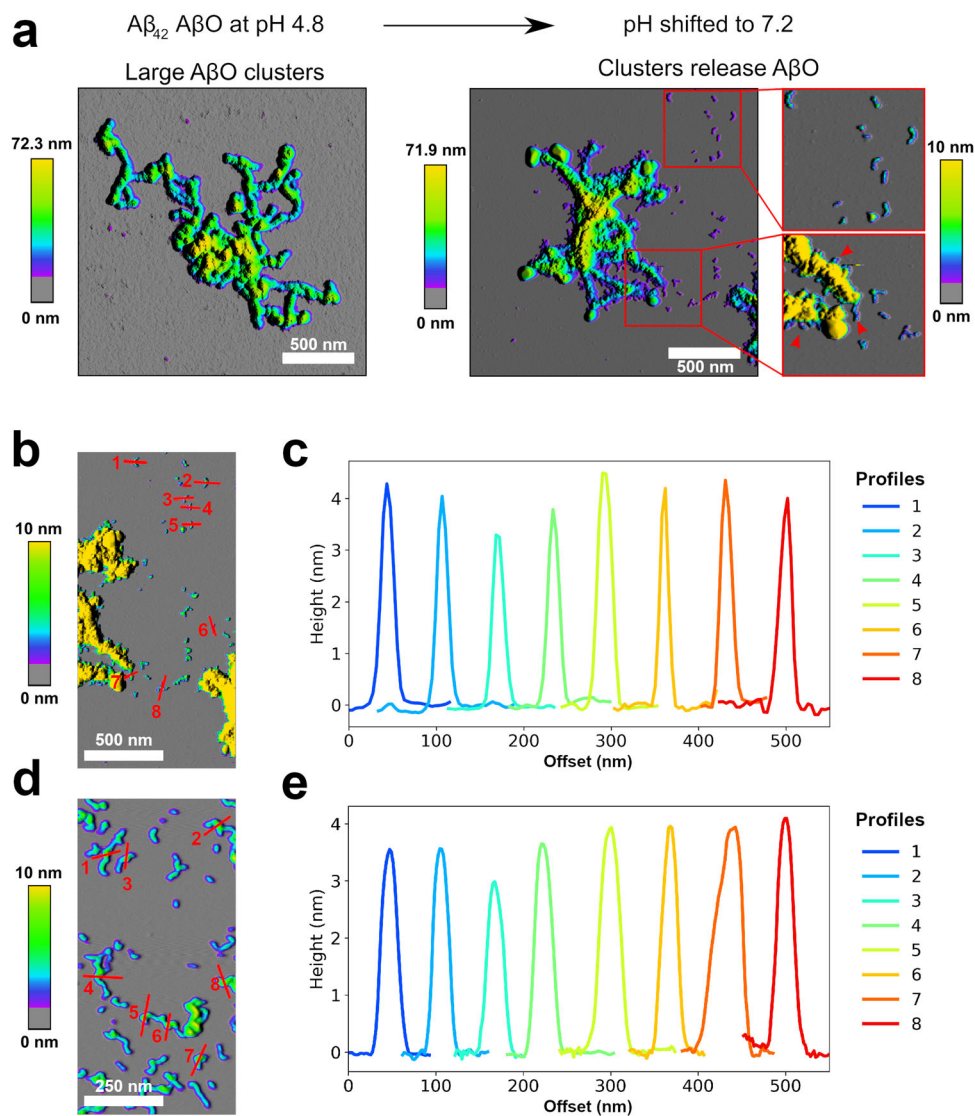


**Fig. 8** Stability of A $\beta$ O<sub>s</sub> formed by A $\beta$ 42 at endo-lysosomal pH after shifting to neutral pH. **a** AFM images of A $\beta$ O<sub>s</sub> formed by 10  $\mu$ M A $\beta$ 42 at pH 4.5 before (left) and after (right) shift to pH 7.2. Red arrowheads point to a few of the sites where A $\beta$ O<sub>s</sub> seem to detach from A $\beta$ O clusters. In all, 3–7 micrographs were recorded per condition to ensure reproducibility. **b, c** Height profiles of small A $\beta$ O<sub>s</sub> after pH shift to neutral pH. Height profiles in **c** correspond to the sections in **b**. **d, e** Height profiles of A $\beta$ O<sub>s</sub> formed by 110  $\mu$ M A $\beta$ 42 at pH 7.2. Height profiles in **e** correspond to the sections in **d**.

super-resolution imaging to determine the kinetics of A $\beta$  aggregation in live cells and found that aggregation occurred in endo-lysosomal compartments<sup>41</sup>. Importantly, they reported that A $\beta$ 42 aggregated without a lag time into compact, dense structures<sup>41</sup>. Both the absence of a lag time and the structural characterization are in line with the low pH A $\beta$ O clusters described here, suggesting that A $\beta$ O clusters indeed form in endo-lysosomal compartments and represent the dominant A $\beta$  aggregate species in live cells. Subsequently, A $\beta$ O<sub>s</sub> might cause lysosomal impairment, leak into the cytosol and cause intracellular damage, or might be secreted and spread to neighboring cells, where they could contribute to the propagation of pathology<sup>40,42,44–46,48,49</sup>.

Enhanced aggregation at acidic pH is a known property of A $\beta$  with established relevance for sample preparation<sup>63</sup>. Our results are in line with a study on the aggregation of A $\beta$ 40 (at a concentration of 230  $\mu$ M) at pH 5.8 that reported the rapid formation of large clusters with (proto)fibrillar and globular substructures that were not able to seed, but rather inhibited, amyloid fibril formation<sup>53</sup>. Our analysis of the aggregation kinetics reveals that these low pH A $\beta$  aggregates, often termed amorphous aggregates,

form along the same pathway as neutral pH A $\beta$ O<sub>s</sub> and therefore represent particle aggregates of A $\beta$ O<sub>s</sub>. This is supported by the observation that low pH A $\beta$ O clusters release spherical and curvilinear A $\beta$ O<sub>s</sub> upon a shift to neutral pH (Fig. 8a). Nevertheless, there may be differences between atomic-level structures and between intermolecular interactions in A $\beta$ O<sub>s</sub> formed at different pH, just as atomic-level structures and protofilament interfaces of amyloid fibril polymorphs can differ significantly.

The increasing clustering of A $\beta$ O<sub>s</sub> upon pH reduction from neutral to pH 6 points to the high propensity of A $\beta$ O<sub>s</sub> to associate. At neutral pH, self-association of spherical A $\beta$ O<sub>s</sub> results in annular and compact assemblies and finally to large A $\beta$ O clusters (Fig. 6). This propensity of A $\beta$ O<sub>s</sub> to associate likely also contributes to their clustering with neuronal receptors<sup>35,36</sup> and to their accumulation around amyloid fibril plaques<sup>66</sup>.

In contrast to A $\beta$ O formation, amyloid fibril formation of dimA $\beta$  is slowed down at acidic pH. This pH dependence is not an inherent property of A $\beta$  amyloid fibril formation: in the absence of A $\beta$ O<sub>s</sub>, A $\beta$ 42 amyloid fibril formation occurs rapidly at



blank due to the risk of aberrant aggregation behavior. The plate was put in a BMG ClarioStar plater reader fitted with two injectors and tempered at 37 °C. One syringe of the injector was equilibrated with 1 ml 10× buffer concentrate. The reaction was started using the injector of the plater reader by dispensing 10 µl of the concentrate at highest available speed into each of the wells. This adjusted the pH value in situ and initiated oligomerization. Data points were collected in evenly spaced intervals depending on the velocity of the reaction using the BMG Reader Control software (version 5.40).

For shifting the pH in situ twice, both syringes were equilibrated with 10× buffer concentrate; the first one resulting in a final buffer concentration of 20 mM and pH 4.5 and the second one resulting in a final buffer concentration of 50 mM and pH 7.2. The first syringe was used to inject 10 µl to initiate oligomerization, whereas the second one was used to inject 11 µl to achieve the shift to neutral pH at a time point where the oligomerization reaction had reached its plateau.

For analysis of the kinetics of AβO formation, the initial phase of the ThT kinetics was fit to one-step oligomerization  $nM \rightarrow M_n$  (ref. 11). The AβO mass concentration,  $M_{A\beta O}$ , evolves in time according to the following expression

$$M_{A\beta O}(t) = M_0 - [M_0^{1-n} + (n-1)knt]^{1/(1-n)} \quad (1)$$

with  $M_0$  the total protein concentration,  $k$  the oligomerization rate constant, and  $n$  the oligomer size or reaction order. Global fits to the pH- and concentration-dependent AβO formation data were performed using the Origin 9.0 software with a reaction order of  $n = 3$  shared between all data sets, and the oligomerization rate constant  $k$  as a pH-dependent parameter, which was shared within the concentration-dependency data sets at a given pH. The proportionality constant relating  $M(t)$  to ThT fluorescence intensity was treated as a fit parameter with an individual value for every sample.

**Atomic force microscopy.** In all, 10 µl of the dimAβ samples were taken directly from the plate after the ThT assays at a concentration of 5 µM and applied onto freshly cleaved muscovite mica. They were left to dry, washed with 500 µl ddH<sub>2</sub>O, and dried with a stream of N<sub>2</sub> gas. For imaging dimAβ at pH 4.8, the aforementioned method did not work, likely due to sticking of the sample to the well. Instead, all reaction components apart from the buffer concentrate were premixed and loaded into a micropipette tip. By adding the reaction components to a vial containing the buffer concentrate and thorough mixing, the reaction was started, before pulling the solution back into the tip. Immediately afterwards, the micropipette was relocated into a 37 °C incubation cabinet, where a drop was pushed onto the point where it still stuck to the tip. After 45 s, the drop was pushed onto the freshly cleaved muscovite mica and preparation commenced as with the other pH values.

For the Aβ42 samples, 5 µl of the respective concentrations were taken, applied onto freshly cleaved muscovite mica, and left to dry for 15 min before carefully washing with 200 µl ddH<sub>2</sub>O and drying under a stream of N<sub>2</sub> gas.

Imaging was performed in intermittent contact mode (AC mode) in a JPK Nano Wizard 3 atomic force microscope (JPK, Berlin) using a silicon cantilever with silicon tip (OMCL-AC160TS-R3, Olympus) with a typical tip radius of  $9 \pm 2$  nm, a force constant of 26 N/m, and resonance frequency around 250 kHz. The images were processed using the JPK DP Data Processing Software (version spm-5.0.84). For the presented height profiles, a polynomial fit was subtracted from each scan line first independently and then using limited data range. False-color height images were overlaid onto the amplitude profile.

Particle height distributions were extracted from AFM images. Therefore, the Morphological Active Contours without Edges (MorphACWE) function of python's scikit-image module was used to distinguish and separate AβOs from background (see Supplementary Fig. 10 for examples of AFM image segmentation). Histogramical height profiles of AβOs at different pH were determined as per pixel heights of the MorphACWE-isolated areas.

**Cryo-EM.** For cryo-EM imaging, the AβO sample was plunge-frozen on glow-discharged Quantifoil 1.2/1.3 grids. In total, 1308 micrographs were recorded as focal pairs at high defocus (6 µm) and low defocus (using a range of  $-0.5$  to  $-2$  µm) on a Tecnai Arctica (200 kV) using a Falcon III direct electron detector, yielding a pixel size of 0.935 Å. Particle selection was performed automatically using cryOLO<sup>68</sup>. In total, 32,211 particles were selected on the high defocus micrographs. The contrast transfer function of the micrographs was determined using CTFIND4<sup>69</sup>. Further image processing was performed using the software package RELION 3.0.5<sup>70</sup>. Two-dimensional and 3D classification was conducted on the high-defocus images to clean the data set. A box size of 128 pix, which corresponds to 119.7 Å, and a radial mask with a diameter of 100 Å were used.

The high-defocus micrographs were aligned to the low-defocus micrographs. The relative shifts obtained from this alignment were applied to all particles (that were picked from the high-defocus micrographs) and then the particles were extracted from the low-defocus micrographs with the shifted particle coordinates, while keeping the Euler angles from the high-defocus 3D refinements. A 3D reconstruction calculated from the high-defocus images was low-pass filtered to 60 Å and was used as an initial model for further low-defocus 3D refinements. For further processing steps, only micrographs that contain a signal beyond a resolution of 5 Å were used. The final resolution of 17 Å was assessed by Fourier shell correlation.

In order to obtain an estimate for the molecular mass within the reconstructed density, 110 pseudo-atomic models with varying number of pseudo-atoms (molecular masses between 10 and 120 kDa) were generated from the density map using the program VISDEM<sup>71</sup>, which is part of the software package DireX<sup>72</sup>. In VISDEM, atoms are randomly placed into a density region with density above a provided threshold. The density threshold was set to yield a volume such that the mass density is fixed at 0.714 ml/g (average mass density observed in proteins). The pseudo-atomic model has a composition of 62.2% C atoms, 20.6% O atoms, and 17.2% N atoms, which corresponds to the average composition observed in proteins. Afterwards, a density map was computed from each of the 110 pseudo-atomic models. The VISDEM method was used to sharpen these pseudo-atomic model maps as well as the EM reconstruction. The sharpening was performed with a resolution cutoff of 17 Å and the mass of the corresponding pseudo-atomic model. Finally, the cross-correlation between the sharpened EM reconstruction and the sharpened pseudo-atomic model map was computed and plotted for each tested mass. The highest cross-correlation was found for the pseudo-atomic model map that contains a molecular mass of 62 kDa. One dimAβ monomer (101 amino acids) has a molecular mass of 10.0 kDa. Thus, the reconstructed density likely holds six dimAβ monomers. The final 3D reconstruction of the oligomer was sharpened by VISDEM using a mass of 62 kDa and a resolution cutoff of 17 Å.

#### Preparation of dimAβ AβOs and Aβ40 monomers for treatment of primary neurons.

Aβ preparations were performed under sterile conditions. DimAβ lyophilisate was resuspended in 50 mM NaOH until completely dissolved. Next, phosphate-buffered saline (PBS) and 50 mM HCl were added and immediately mixed, obtaining a final concentration of 20 µM dimAβ and 40 µM Aβ40. To induce AβO formation, dimAβ was incubated at 37 °C for 16 h. Aβ40 controls were prepared in the same manner without subsequent incubation. Primary neurons (DIV15–22) were treated with either 0.5 µM dimAβ AβO or 1 µM Aβ40 monomers diluted in conditioned neuronal maintenance media for 3 and 24 h under normal growth conditions (see below). In addition, control cells were treated with a vehicle control (PBS containing 50 mM NaOH and 50 mM HCl). Afterwards, cells were fixed and stained as described below.

**Primary neuron culture.** Primary neurons were isolated and cultured as described before<sup>73</sup> with slight modifications: In brief, the brains of FVB/N mouse embryos were dissected at embryonic day 13.5. Brainstem and meninges were removed and whole cortex was digested with 1× Trypsin (Panbiotech). Neurons were diluted in pre-warmed (37 °C) neuronal plating medium (Neurobasal media (ThermoFisher Scientific), 1% fetal bovine serum (FBS; Biochrom AG), 1× antibiotic/antimycotic solution (ThermoFisher Scientific), 1× NS21 (Panbiotech)) and seeded onto poly-D-lysine (Merck) coated coverslips. Neurons were cultivated in a humidified incubator at 37 °C, 5% CO<sub>2</sub>. Four days after plating, media was doubled with neuronal maintenance media (Neurobasal media (ThermoFisher Scientific), 1× antibiotic/antimycotic solution (ThermoFisher Scientific), 1× NS21 (Panbiotech)) and cells were treated with 0.5 µg/ml Cytosine β-D-arabinofuranoside (AraC; Sigma-Aldrich). The isolation of primary neurons was reviewed and approved (§4 TschG) by the Animal Welfare Officer of University of Cologne and the Landesamt für Natur-, Umwelt- und Verbraucherschutz (LANUV), Germany.

**Somatodendritic missorting of Tau.** To analyze Tau somatodendritic localization, neurons were fixed with 3.7% formaldehyde/4% sucrose in PBS (both Sigma-Aldrich) for 30 min at RT using gentle agitation after treatment with Aβ or vehicle control for the indicated time points. Afterwards, cells were permeabilized and blocked for 5–10 min in 5% bovine serum albumin/0.2% TX-100 in PBS (both Carl Roth), washed with PBS, and stained with a polyclonal rabbit anti-Tau (K9JA, Dako A0024; dilution: 1:1000) antibody overnight at 4 °C. The next day, coverslips were washed again with PBS, incubated with NucBlue (ThermoFisher Scientific) for 15 min, and subsequently stained with a secondary antibody coupled to an AlexaFluor dye (ThermoFisher Scientific) for 1 h at RT. Coverslips were mounted onto glass slides using Aqua-Poly/Mount (Polysciences) and dried overnight at RT (for further details on immunofluorescence staining procedure, see ref. 73). Images of neuronal cell bodies were taken with a wide-field fluorescence microscope (Axioscope 5, Zeiss) and the ZenBlue Pro imaging software (V2.5, Zeiss). Fluorescence intensities of cell bodies were quantified using the ImageJ software<sup>74,75</sup>. Fluorescence intensity values were normalized to vehicle-treated control cells after 3 h of treatment. All experiments were performed 4 times; 30 cells were analyzed for each condition. Statistical analysis was done by two-way analysis of variance (ANOVA) with Tukey's test for multiple comparisons using GraphPad Prism v6 (GraphPad Software).

**Cytotoxic effect of dimAβ.** To evaluate AβO toxicity, cells were fixed and stained with NucBlue (ThermoFisher Scientific) after dimAβ AβO treatment. Shape and density of nuclei were analyzed and counted: cells were considered dead, when nuclei appeared condensed and smaller, compared to viable cell nuclei. All experiments were conducted for 3 times; around 300 nuclei were analyzed for each condition. Statistical analysis was done by two-way ANOVA with Tukey's test for multiple comparisons using GraphPad Prism v6 (GraphPad Software).

**A $\beta$  targeting to postsynaptic spines and imaging of spontaneous calcium oscillations.** To analyze A $\beta$  binding to synapses, neurons were fixed and stained for F-actin with phalloidin as a marker of synaptic spines (ThermoFisher Scientific) and a monoclonal mouse anti-A $\beta$  (clone 4G8, Merck, #MAB1561; dilution: 1:300) antibody. The experiment was repeated independently for four times and colocalization of A $\beta$ O with synapses was observed for all replicates.

To monitor spontaneous Ca<sup>2+</sup> oscillations, primary neurons were labeled with 2  $\mu$ M Fluo-4 (ThermoFisher Scientific) and 0.02% Pluronic F127 (Merck) for 20 min after 24 h of dimA $\beta$  treatment. Time-lapse movies of different fields were recorded for 1 min each (frame rate: 1 s) using a Leica DMi8 microscope (Leica) and the Leica LAS X imaging software (v3.7.3). Fluorescence intensity changes of cell bodies were quantified over time with ImageJ<sup>74,75</sup> and corrected for background signal. Fluorescence intensities were normalized to minimum values and peaks per minute were counted for each sample. In total, 35 cells were analyzed; statistical analysis was done by two-tailed unpaired *t* test.

**Preparation of fluorescently labeled A $\beta$  for cell culture experiments.** For preparation of AbberiorStar 520SXP-labeled Cys0-dimA $\beta$ , a mutant of dimA $\beta$  with an N-terminal cysteine residue was expressed as described above. For fluorophore labeling, TCEP-reduced Cys0-dimA $\beta$  lyophilisate was incubated in 200 mM HEPES pH 7.0 with a twofold molar excess of maleimide-conjugated AbberiorStar 520SXP fluorophore, which was dissolved in dimethylformamide. After 2 h of incubation, the labeled dimA $\beta$  was purified using reverse-phase HPLC. Samples were lyophilized, redissolved in HFIP, and aliquots were prepared. These aliquots were lyophilized and stored at RT for later use. Abberior STAR 520SXP-labeled A $\beta$ O were prepared from a 1:10 molar ratio of Abberior STAR 520SXP-labeled dimA $\beta$  and unlabeled dimA $\beta$ , in order to avoid that the fluorophore alters A $\beta$ O properties. In all, 10  $\mu$ l of 1:10 mixture of Abberior STAR 520SXP-labeled dimA $\beta$  and unlabeled dimA $\beta$  was prepared in 50 mM NaOH. Quickly, 490  $\mu$ l phenol red-free Dulbecco's Modified Eagle's Medium (DMEM) supplemented with 100 U/ml penicillin–streptomycin was added, and the pH was readjusted by adding 10  $\mu$ l 50 mM HCl. The final dimA $\beta$  concentration was 10  $\mu$ M. The sample was quietly incubated at 37 °C in the dark for 24 h. A $\beta$ O formation was confirmed using AFM.

For A $\beta$ 42 cell culture experiments, A $\beta$ 42-HiLyte Fluor 647 (Anaspec) was dissolved in HFIP and lyophilized into smaller aliquots (30  $\mu$ g). For cell culture experiments, aliquots were first dissolved in 3  $\mu$ l 50 mM NaOH. In all, 544  $\mu$ l phenol red-free DMEM supplemented with 100 U/ml penicillin–streptomycin was added, and the pH was recalibrated by the addition of 3  $\mu$ l 50 mM HCl. To avoid exposure of the A $\beta$  peptide to local low pH environments, the HCl was pipetted into the lid of the tube, closed, and quickly vortexed. This procedure yields a 10  $\mu$ M mostly monomeric stock solution of A $\beta$ 42-HiLyte Fluor 647 suitable for cell culture experiments.

**Neuroblastoma cell culture.** SH-SY5Y cells were grown to 80% confluency in DMEM with phenol red, 10% FBS, and 100 U/ml penicillin–streptomycin in T75 flasks. Experiments were performed in Ibidi collagen IV-coated  $\mu$ -Slide VI 0.4. A total of 7500 cells (250,000 cells/ml) were seeded into each channel of the slide. Cells adhered to the surface of the channels within an hour of incubation at 37 °C, 5% CO<sub>2</sub>, in a humidified chamber. Subsequently, the feeding reservoirs of the channels were filled with further medium. Each day, the medium in the reservoirs was replaced with fresh medium until the cell density was satisfactory for coin-cubation experiments.

**Coincubation experiments and imaging.** For coincubation and imaging experiments, phenol red was removed by flushing the channels three times with phenol red-free DMEM supplemented with 100 U/ml penicillin–streptomycin. Subsequently, channels were filled with medium containing corresponding A $\beta$  species. Cells were incubated for 24 h. Channels were flushed with fresh medium and supplemented with 50 nM Yellow HCK-123 LysoTracker. Imaging was performed either on a Leica Infinity TIRF microscope or on a confocal microscope using the Leica LAS AF software. Confocal measurements were performed using a TCS SP8 STED 3 $\times$  (Leica Microsystems) equipped with an HC PL APO CS2  $\times$ 100 objective (NA 1.4) at a scan speed of 600 Hz and a line accumulation of 6. A 488 nm of a pulsed white light laser was chosen as excitation for Yellow HCK-123 LysoTracker and AbberiorSTAR520XPS. The emitted fluorescent signal was detected by counting-mode hybrid detectors in the spectral range of 500–531 nm for Yellow HCK-123 LysoTracker and 650–765 nm for AbberiorStar520SXP. Additionally, a time-gating of 0.1 ns was used to avoid laser reflection.

**Reporting summary.** Further information on research design is available in the Nature Research Reporting Summary linked to this article.

## Data availability

The cryo-EM density map of dimA $\beta$  A $\beta$ O has been deposited in the Electron Microscopy Data Bank under accession code [EMD-11327](https://doi.org/10.1038/EMD-11327). The authors declare that all the data necessary to interpret, verify, and extend the research of the article are available within the article (and Supplementary Information files). All data are available from the corresponding authors on reasonable request. Source data are provided with this paper.

Received: 1 July 2020; Accepted: 14 July 2021;

Published online: 30 July 2021

## References

- Gremer, L. et al. Fibril structure of amyloid- $\beta$ (1-42) by cryo-electron microscopy. *Science* **358**, 116–119 (2017).
- Kollmer, M. et al. Cryo-EM structure and polymorphism of A $\beta$  amyloid fibrils purified from Alzheimer's brain tissue. *Nat. Commun.* **10**, 4760 (2019).
- Selkoe, D. J. & Hardy, J. The amyloid hypothesis of Alzheimer's disease at 25 years. *EMBO Mol. Med.* **8**, 595–608 (2016).
- Cline, E. N., Bicca, M. A., Viola, K. L. & Klein, W. L. The Amyloid- $\beta$  oligomer hypothesis: beginning of the third decade. *J. Alzheimers Dis.* **64**, S567–S610 (2018).
- Ono, K. & Tsuji, M. Protofibrils of amyloid- $\beta$  are important targets of a disease-modifying approach for Alzheimer's disease. *Int. J. Mol. Sci.* **21**, 952 (2020).
- Chromy, B. A. et al. Self-assembly of A $\beta$ (1-42) into globular neurotoxins. *Biochemistry* **42**, 12749–12760 (2003).
- Jan, A., Hartley, D. M. & Lashuel, H. A. Preparation and characterization of toxic A $\beta$  aggregates for structural and functional studies in Alzheimer's disease research. *Nat. Protoc.* **5**, 1186–1209 (2010).
- Lambert, M. P. et al. Diffusible, nonfibrillar ligands derived from A $\beta$ 1-42 are potent central nervous system neurotoxins. *Proc. Natl Acad. Sci. USA* **95**, 6448–6453 (1998).
- Walsh, D. M. et al. Amyloid  $\beta$ -protein fibrillogenesis. Structure and biological activity of protofibrillar intermediates. *J. Biol. Chem.* **274**, 25945–25952 (1999).
- Walsh, D. M., Lomakin, A., Benedek, G. B., Condron, M. M. & Teplow, D. B. Amyloid  $\beta$ -protein fibrillogenesis. Detection of a protofibrillar intermediate. *J. Biol. Chem.* **272**, 22364–22372 (1997).
- Hasecke, F. et al. Origin of metastable oligomers and their effects on amyloid fibril self-assembly. *Chem. Sci.* **9**, 5937–5948 (2018).
- Bitan, G., Fradinger, E. A., Spring, S. M. & Teplow, D. B. Neurotoxic protein oligomers—what you see is not always what you get. *Amyloid* **12**, 88–95 (2005).
- Kodali, R. & Wetzel, R. Polymorphism in the intermediates and products of amyloid assembly. *Curr. Opin. Struct. Biol.* **17**, 48–57 (2007).
- Cohen, S. I. et al. Proliferation of amyloid- $\beta$ 42 aggregates occurs through a secondary nucleation mechanism. *Proc. Natl Acad. Sci. USA* **110**, 9758–9763 (2013).
- Michaels, T. C. T. et al. Dynamics of oligomer populations formed during the aggregation of Alzheimer's A $\beta$ 42 peptide. *Nat. Chem.* **12**, 445–451 (2020).
- Sehlin, D. et al. Large aggregates are the major soluble A $\beta$  species in AD brain fractionated with density gradient ultracentrifugation. *PLoS ONE* **7**, e32014 (2012).
- Fowler, S. W. et al. Genetic modulation of soluble A $\beta$  rescues cognitive and synaptic impairment in a mouse model of Alzheimer's disease. *J. Neurosci.* **34**, 7871–7885 (2014).
- Lacor, P. N. et al. A $\beta$  oligomer-induced aberrations in synapse composition, shape, and density provide a molecular basis for loss of connectivity in Alzheimer's disease. *J. Neurosci.* **27**, 796–807 (2007).
- Forny-Germano, L. et al. Alzheimer's disease-like pathology induced by amyloid- $\beta$  oligomers in nonhuman primates. *J. Neurosci.* **34**, 13629–13643 (2014).
- Hartley, D. M. et al. Protofibrillar intermediates of amyloid  $\beta$ -protein induce acute electrophysiological changes and progressive neurotoxicity in cortical neurons. *J. Neurosci.* **19**, 8876–8884 (1999).
- Yasumoto, T. et al. High molecular weight amyloid  $\beta$ 1-42 oligomers induce neurotoxicity via plasma membrane damage. *FASEB J.* **33**, 9220–9234 (2019).
- Klyubin, I. et al. Soluble Arctic amyloid  $\beta$  protein inhibits hippocampal long-term potentiation in vivo. *Eur. J. Neurosci.* **19**, 2839–2846 (2004).
- Tomiyama, T. et al. A mouse model of amyloid  $\beta$  oligomers: their contribution to synaptic alteration, abnormal tau phosphorylation, glial activation, and neuronal loss in vivo. *J. Neurosci.* **30**, 4845–4856 (2010).
- De Felice, F. G. et al. A $\beta$  oligomers induce neuronal oxidative stress through an N-methyl-D-aspartate receptor-dependent mechanism that is blocked by the Alzheimer drug memantine. *J. Biol. Chem.* **282**, 11590–11601 (2007).
- Maezawa, I., Zimin, P. I., Wulff, H. & Jin, L. W. Amyloid- $\beta$  protein oligomer at low nanomolar concentrations activates microglia and induces microglial neurotoxicity. *J. Biol. Chem.* **286**, 3693–3706 (2011).
- Paranjape, G. S., Gouwens, L. K., Osborn, D. C. & Nichols, M. R. Isolated amyloid- $\beta$ (1-42) protofibrils, but not isolated fibrils, are robust stimulators of microglia. *ACS Chem. Neurosci.* **3**, 302–311 (2012).
- Söllvander, S. et al. Accumulation of amyloid- $\beta$  by astrocytes result in enlarged endosomes and microvesicle-induced apoptosis of neurons. *Mol. Neurodegener.* **11**, 38 (2016).

28. Umeda, T. et al. Intraneuronal amyloid  $\beta$  oligomers cause cell death via endoplasmic reticulum stress, endosomal/lysosomal leakage, and mitochondrial dysfunction in vivo. *J. Neurosci. Res.* **89**, 1031–1042 (2011).
29. Zempel, H. & Mandelkow, E. Lost after translation: missorting of Tau protein and consequences for Alzheimer disease. *Trends Neurosci.* **37**, 721–732 (2014).
30. Lord, A. et al. Amyloid- $\beta$  protofibril levels correlate with spatial learning in Arctic Alzheimer's disease transgenic mice. *FEBS J.* **276**, 995–1006 (2009).
31. Tomiyama, T. et al. A new amyloid  $\beta$  variant favoring oligomerization in Alzheimer's-type dementia. *Ann. Neurol.* **63**, 377–387 (2008).
32. Kutzsche, J. et al. Safety and pharmacokinetics of the orally available antiprionic compound PRI-002: a single and multiple ascending dose phase I study. *Alzheimers Dement.* **6**, e12001 (2020).
33. Logovinsky, V. et al. Safety and tolerability of BAN2401—a clinical study in Alzheimer's disease with a protofibril selective A $\beta$  antibody. *Alzheimers Res. Ther.* **8**, 14 (2016).
34. Overk, C. R. & Masliah, E. Toward a unified therapeutics approach targeting putative amyloid- $\beta$  oligomer receptors. *Proc. Natl Acad. Sci. USA* **111**, 13680–13681 (2014).
35. Jarosz-Griffiths, H. H., Noble, E., Rushworth, J. V. & Hooper, N. M. Amyloid- $\beta$  receptors: the good, the bad, and the prion protein. *J. Biol. Chem.* **291**, 3174–3183 (2016).
36. Rösener, N. S. et al. A d-enantiomeric peptide interferes with heteroassociation of amyloid- $\beta$  oligomers and prion protein. *J. Biol. Chem.* **293**, 15748–15764 (2018).
37. De Felice, F. G. et al. Alzheimer's disease-type neuronal tau hyperphosphorylation induced by A $\beta$  oligomers. *Neurobiol. Aging* **29**, 1334–1347 (2008).
38. Zempel, H. et al. Amyloid- $\beta$  oligomers induce synaptic damage via Tau-dependent microtubule severing by TTL6 and spastin. *EMBO J.* **32**, 2920–2937 (2013).
39. Zempel, H., Thies, E., Mandelkow, E. & Mandelkow, E. M. A $\beta$  oligomers cause localized Ca(2+) elevation, missorting of endogenous Tau into dendrites, Tau phosphorylation, and destruction of microtubules and spines. *J. Neurosci.* **30**, 11938–11950 (2010).
40. LaFerla, F. M., Green, K. N. & Oddo, S. Intracellular amyloid- $\beta$  in Alzheimer's disease. *Nat. Rev. Neurosci.* **8**, 499–509 (2007).
41. Esbjörner, E. K. et al. Direct observations of amyloid  $\beta$  self-assembly in live cells provide insights into differences in the kinetics of A $\beta$ (1–40) and A $\beta$ (1–42) aggregation. *Chem. Biol.* **21**, 732–742 (2014).
42. Orr, M. E. & Oddo, S. Autophagic/lysosomal dysfunction in Alzheimer's disease. *Alzheimers Res. Ther.* **5**, 53 (2013).
43. Rushworth, J. V., Griffiths, H. H., Watt, N. T. & Hooper, N. M. Prion protein-mediated toxicity of amyloid- $\beta$  oligomers requires lipid rafts and the transmembrane LRP1. *J. Biol. Chem.* **288**, 8935–8951 (2013).
44. Hu, X. et al. Amyloid seeds formed by cellular uptake, concentration, and aggregation of the amyloid- $\beta$  peptide. *Proc. Natl Acad. Sci. USA* **106**, 20324–20329 (2009).
45. Soura, V. et al. Visualization of co-localization in A $\beta$ 42-administered neuroblastoma cells reveals lysosome damage and autophagosome accumulation related to cell death. *Biochem. J.* **441**, 579–590 (2012).
46. Marshall, K. E., Vadukul, D. M., Staras, K. & Serpell, L. C. Misfolded amyloid- $\beta$ –42 impairs the endosomal-lysosomal pathway. *Cell. Mol. Life Sci.* **77**, 5031–5043 (2020).
47. Koo, E. H. & Squazzo, S. L. Evidence that production and release of amyloid  $\beta$ -protein involves the endocytic pathway. *J. Biol. Chem.* **269**, 17386–17389 (1994).
48. Sannerud, R. et al. Restricted location of PSEN2/ $\gamma$ -secretase determines substrate specificity and generates an intracellular A $\beta$  pool. *Cell* **166**, 193–208 (2016).
49. Vadukul, D. M. et al. Internalisation and toxicity of amyloid- $\beta$  1–42 are influenced by its conformation and assembly state rather than size. *FEBS Lett.* **594**, 3490–3503 (2020).
50. Lord, A. et al. The Arctic Alzheimer mutation facilitates early intraneuronal A $\beta$  aggregation and senile plaque formation in transgenic mice. *Neurobiol. Aging* **27**, 67–77 (2006).
51. Yang, A. J., Chandswangbhuvana, D., Margol, L. & Glabe, C. G. Loss of endosomal/lysosomal membrane impermeability is an early event in amyloid A $\beta$ 1–42 pathogenesis. *J. Neurosci. Res.* **52**, 691–698 (1998).
52. Meisl, G. et al. Molecular mechanisms of protein aggregation from global fitting of kinetic models. *Nat. Protoc.* **11**, 252–272 (2016).
53. Wood, S. J., Maleeff, B., Hart, T. & Wetzel, R. Physical, morphological and functional differences between ph 5.8 and 7.4 aggregates of the Alzheimer's amyloid peptide A $\beta$ . *J. Mol. Biol.* **256**, 870–877 (1996).
54. Fu, Z., Aucoin, D., Davis, J., Van Nostrand, W. E. & Smith, S. O. Mechanism of nucleated conformational conversion of A $\beta$ 42. *Biochemistry* **54**, 4197–4207 (2015).
55. Barghorn, S. et al. Globular amyloid  $\beta$ -peptide oligomer - a homogenous and stable neuropathological protein in Alzheimer's disease. *J. Neurochem.* **95**, 834–847 (2005).
56. Gong, Y. et al. Alzheimer's disease-affected brain: presence of oligomeric A $\beta$  ligands (ADDLs) suggests a molecular basis for reversible memory loss. *Proc. Natl Acad. Sci. USA* **100**, 10417–10422 (2003).
57. Lesne, S. et al. A specific amyloid- $\beta$  protein assembly in the brain impairs memory. *Nature* **440**, 352–357 (2006).
58. Liu, P. et al. Quaternary structure defines a large class of amyloid- $\beta$  oligomers neutralized by sequestration. *Cell Rep.* **11**, 1760–1771 (2015).
59. Moringa, A. et al. Critical role of interfaces and agitation on the nucleation of A $\beta$  amyloid fibrils at low concentrations of A $\beta$  monomers. *Biochim. Biophys. Acta* **1804**, 986–995 (2010).
60. Carrotta, R., Manno, M., Bulone, D., Martorana, V. & San Biagio, P. L. Protofibril formation of amyloid  $\beta$ -protein at low pH via a non-cooperative elongation mechanism. *J. Biol. Chem.* **280**, 30001–30008 (2005).
61. Zempel, H. & Mandelkow, E. M. Linking amyloid- $\beta$  and tau: amyloid- $\beta$  induced synaptic dysfunction via local wreckage of the neuronal cytoskeleton. *Neurodegener. Dis.* **10**, 64–72 (2012).
62. Kuperstein, I. et al. Neurotoxicity of Alzheimer's disease A $\beta$  peptides is induced by small changes in the A $\beta$ 42 to A $\beta$ 40 ratio. *EMBO J.* **29**, 3408–3420 (2010).
63. Fezoui, Y. et al. An improved method of preparing the amyloid  $\beta$ -protein for fibrillogenesis and neurotoxicity experiments. *Amyloid* **7**, 166–178 (2000).
64. Hackl, E. V., Darkwah, J., Smith, G. & Ermolina, I. Effect of acidic and basic pH on Thioflavin T absorbance and fluorescence. *Eur. Biophys. J.* **44**, 249–261 (2015).
65. Hasecke, F. et al. Protofibril-fibril interactions inhibit amyloid fibril assembly by obstructing secondary nucleation. *Angew. Chem. Int. Ed.* **60**, 3016–3021 (2021).
66. Brody, D. L., Jiang, H., Wildburger, N. & Esparza, T. J. Non-canonical soluble amyloid- $\beta$  aggregates and plaque buffering: controversies and future directions for target discovery in Alzheimer's disease. *Alzheimers Res. Ther.* **9**, 62 (2017).
67. Macao, B. et al. Recombinant amyloid beta-peptide production by coexpression with an affibody ligand. *BMC Biotechnol.* **8**, 82 (2008).
68. Wagner, T. et al. SPHIRE-crYOLO is a fast and accurate fully automated particle picker for cryo-EM. *Commun. Biol.* **2**, 218 (2019).
69. Rohou, A. & Grigorieff, N. CTFIND4: fast and accurate defocus estimation from electron micrographs. *J. Struct. Biol.* **192**, 216–221 (2015).
70. Zivanov, J. et al. New tools for automated high-resolution cryo-EM structure determination in RELION-3. *Elife* **7**, e42166 (2018).
71. Spiegel, M., Duraisamy, A. K. & Schröder, G. F. Improving the visualization of cryo-EM density reconstructions. *J. Struct. Biol.* **191**, 207–213 (2015).
72. Schröder, G. F., Brunger, A. T. & Levitt, M. Combining efficient conformational sampling with a deformable elastic network model facilitates structure refinement at low resolution. *Structure* **15**, 1630–1641 (2007).
73. Zempel, H. & Mandelkow, E. M. Tracking Tau in neurons: how to grow, fix, and stain primary neurons for the investigation of Tau in all developmental stages. *Methods Mol. Biol.* **1523**, 327–334 (2017).
74. Schindelin, J. et al. Fiji: an open-source platform for biological-image analysis. *Nat. Methods* **9**, 676–682 (2012).
75. Schneider, C. A., Rasband, W. S. & Eliceiri, K. W. NIH Image to ImageJ: 25 years of image analysis. *Nat. Methods* **9**, 671–675 (2012).
76. Champion, D., Pottier, C., Nicolas, G., Le Guennec, K. & Rovelet-Lecrux, A. Alzheimer disease: modeling an A $\beta$ -centered biological network. *Mol. Psychiatry* **21**, 861–871 (2016).
77. Hu, Y. B., Dammer, E. B., Ren, R. J. & Wang, G. The endosomal-lysosomal system: from acidification and cargo sorting to neurodegeneration. *Transl. Neurodegener.* **4**, 18 (2015).

## Acknowledgements

This project has received funding from the European Research Council under the European Union's Horizon 2020 research and innovation program, grant agreement No. 726368. We acknowledge support from the Hans und Ilse Breuer-Stiftung, the Else-Kröner-Fresenius Stiftung, and Köln Fortune. We thank Raimond B.G. Ravelli, P.J. Peters, and C. López-Iglesias for advice and helpful discussions; H. Duimel for help with sample preparation; and the M4I Division of Nanoscopy of Maastricht University for microscope access and support. We acknowledge the Center of Advanced Imaging (CAI) at the Heinrich Heine University Düsseldorf for providing access to the TCS SP8 STED 3x and support during image acquisition. WT mice were provided by CMMC animal facility (Cologne, Germany) and CECAD in vivo research facility (Cologne, Germany); live-cell imaging was conducted at the CMMC imaging facility. We thank Jennifer Klimmek for excellent technical support.

## Author contributions

M.P.S., F.H., S.B., G.F.S., H.Z., and W.H. designed the experiments. M.P.S., F.H., S.B., M. Z., S.H., G.F.S., H.Z., and W.H. performed the experiments and analyzed the data. M.P.S., F.H., S.B., M.Z., G.F.S., H.Z., and W.H. wrote the manuscript. All authors commented on the manuscript.

## Funding

Open Access funding enabled and organized by Projekt DEAL.

## Competing interests

The authors declare no competing interests.

**Additional information**

**Supplementary information** The online version contains supplementary material available at <https://doi.org/10.1038/s41467-021-24900-4>.

**Correspondence** and requests for materials should be addressed to H.Z. or W.H.

**Peer review information** *Nature Communications* thanks Jan Bieschke and the other anonymous reviewer(s) for their contribution to the peer review of this work. Peer reviewer reports are available.

**Reprints and permission information** is available at <http://www.nature.com/reprints>

**Publisher's note** Springer Nature remains neutral with regard to jurisdictional claims in published maps and institutional affiliations.



**Open Access** This article is licensed under a Creative Commons Attribution 4.0 International License, which permits use, sharing, adaptation, distribution and reproduction in any medium or format, as long as you give appropriate credit to the original author(s) and the source, provide a link to the Creative Commons license, and indicate if changes were made. The images or other third party material in this article are included in the article's Creative Commons license, unless indicated otherwise in a credit line to the material. If material is not included in the article's Creative Commons license and your intended use is not permitted by statutory regulation or exceeds the permitted use, you will need to obtain permission directly from the copyright holder. To view a copy of this license, visit <http://creativecommons.org/licenses/by/4.0/>.

© The Author(s) 2021